

# Substructure in the stellar halo near the Sun. I. Data-driven clustering in Integrals of Motion space

S. Sofie Lövdal<sup>1</sup>, Tomás Ruiz-Lara<sup>1</sup>, Helmer H. Koppelman<sup>2</sup>, Tadafumi Matsuno<sup>1</sup>, Emma Dodd<sup>1</sup> and Amina Helmi<sup>1</sup>

<sup>1</sup> Kapteyn Astronomical Institute, University of Groningen, Landleven 12, 9747 AD Groningen, The Netherlands  
e-mail: s.s.lovdal@rug.nl

<sup>2</sup> School of Natural Sciences, Institute for Advanced Study, 1 Einstein Drive, Princeton, NJ 08540, USA

January 11, 2022

## ABSTRACT

**Context.** Merger debris is expected to populate the stellar halos of galaxies. In the case of the Milky Way, such debris should be apparent as clumps in a space defined by the stars’ orbital Integrals of Motion.

**Aims.** Our aim is to develop a data-driven and statistically based method for finding such clumps in Integrals of Motion space for nearby halo stars and evaluating their significance robustly.

**Methods.** We use data from *Gaia* EDR3 extended with radial velocities from ground-based spectroscopic surveys to construct a sample of halo stars within 2.5 kpc from the Sun. We apply a hierarchical clustering method that makes exhaustive use of the single linkage algorithm in a 3D space defined by the commonly used integrals of motion energy  $E$ , together with two components of the angular momentum,  $L_z$  and  $L_\perp$ . To evaluate the statistical significance of the clusters found, we compare the density within an ellipsoidal region centered on the cluster to that of random sets with similar global dynamical properties. By picking out the signal at the location of their maximum statistical significance in the hierarchical tree, we extract a set of significant unique clusters. By describing these clusters with ellipsoids, we estimate the proximity of a star to the cluster center using the Mahalanobis distance. Additionally, we apply the HDBSCAN clustering algorithm in velocity space to each cluster to extract subgroups representing debris with different orbital phases.

**Results.** Our procedure identifies 67 highly significant clusters ( $> 3\sigma$ ), containing 12% of the sources in our halo set, and in total 232 subgroups or individual streams in velocity space. In total, 13.8% of the stars in our data set can be confidently associated to a significant cluster based on their Mahalanobis distance. Inspection of the hierarchical tree describing our data set reveals a complex web of relationships between the significant clusters, suggesting that they can be tentatively grouped into at least 6 main large structures, many of which can be associated to previously identified halo substructures, and a number of independent substructures. This preliminary conclusion is further explored in an accompanying paper by Ruiz-Lara et al. (2022), where we also characterize the substructures in terms of their stellar populations.

**Conclusions.** Our method allows us to systematically detect kinematic substructures in the Galactic stellar halo with a data-driven and interpretable algorithm. The list of the clusters and the associated star catalogue are provided in two tables in electronic format.

**Key words.** Galaxy: kinematics and dynamics – Galaxy: formation – Galaxy: halo – solar neighborhood – Galaxy: evolution – Methods: data analysis

## 1. Introduction

According to the  $\Lambda$  cold dark matter model, galaxies grow hierarchically by merging with smaller structures (Springel et al. 2005). In the Milky Way footprints from such events have been predicted to be observable particularly in the stellar halo (see e.g. Helmi 2020), since mergers generally deposit their debris in this component. Thanks to wide-field photometric surveys, large spatially coherent overdensities and numerous stellar streams have been detected in the outer halo (here defined to be beyond 20 kpc from the Galactic centre); see for example Ivezić et al. (2000); Yanny et al. (2000); Majewski et al. (2003); Belokurov et al. (2006); Bernard et al. (2016) and also Mateu et al. (2018) for a compilation. In the inner halo, it was the advent of large samples with phase-space information from the *Gaia* mission (Prusti et al. 2016; Gaia Collaboration et al. 2018b) that enabled the discovery of several kinematic substructures, particularly in the vicinity of the Sun. One of the most significant substructures both because of its extent and its importance, is the debris

from a large object accreted roughly 10 Gyr ago, named *Gaia*-Enceladus (Helmi et al. 2018, see also Belokurov et al. 2018), and which has been estimated to comprise  $\sim 40\%$  of the halo near the Sun. In addition, a hot thick disk (Helmi et al. 2018; Di Matteo et al. 2019), now also known as the “splash” (Belokurov et al. 2020) is similarly dominant amongst stars near the Sun with halo-like kinematics. The remaining substructures are more modest in size, and likely correspond to much smaller accreted systems (see e.g. Yuan et al. 2020b).

The main goal behind the identification of such substructures is to determine and characterize the merger history of the Milky Way. The identification of the various events allows putting constraints on the number of accreted galaxies, their time of accretion, and their internal characteristics, such as for example, their star formation and chemical evolution history, their mass and luminosity, and the presence of associated globular clusters (e.g. Myeong et al. 2018; Massari et al. 2019). The characterization of the building blocks is interesting from a cosmological and galaxy formation perspective, as it allows for example the deter-

mination of the luminosity function across cosmic time. Furthermore, the star formation histories and chemical abundance patterns in accreted objects permits distinguishing types of enrichment sites or channels (e.g. super/hypernovae), as well as the initial mass function in different environments. Importantly, many of the high-redshift analogues of the accreted galaxies will not be directly observable in-situ because of their intrinsically faint luminosity, even with JWST, and so access to this population will likely only remain available in the foreseeable future through studies of nearby ancient stars. The ambitious goals of Galactic archaeology require that we are able to identify substructures in a statistically robust way, to ultimately be able to assess incompleteness or biases, as well as to establish which stars are likely members of the various objects identified as this is necessary for their characterization (eventually through detailed spectroscopic follow-up).

Theoretical models and numerical simulations have shown that accreted objects will preserve their coherent orbital configuration long after the structure is completely phase mixed (Helmi & de Zeeuw 2000), even in the fully hierarchical regime of the cosmological assembly process (Gómez et al. 2013; Simpson et al. 2019). One of the best ways to trace accretion events is to observe clustering in the Integrals of Motion describing the orbits of the stars. In an axisymmetric time-independent potential often used Integrals of Motion are the energy  $E$  and angular momentum in the  $z$ -direction  $L_z$ . The component of the angular momentum  $L_\perp (= \sqrt{L_x^2 + L_y^2})$  is often used as well, since stars originating in the same merger event are expected to remain clustered also in this quantity, even though it is not being fully conserved (see e.g. Helmi et al. 1999). Similarly, action space can be used (see e.g. Myeong et al. 2018), with the advantage that actions are adiabatic invariants, and they are less dependent on distance selections (Lane et al. 2021). The actions however, have the drawback that they are more difficult to determine for a generic Galactic potential (except in approximate form, see e.g. Binney & McMillan 2016; Vasiliev 2019).

Establishing the statistical significance of clumps identified by clustering algorithms in such subspaces is not trivial. Thus far, many works have used either manual selection (e.g. Naidu et al. 2020) or clustering algorithms in Integrals of Motion space successfully for identifying stellar streams in the Milky Way halo (Koppelman et al. 2019a; Borsato et al. 2020). In recent years, works using more advanced machine learning to find clusters have also been published (Yuan et al. 2018; Myeong et al. 2018; Borsato et al. 2020). In the case of manual selection, mathematically establishing the validity is difficult and often bypassed. When it comes to machine learning and advanced clustering algorithms, commonly the results are hard to interpret, especially in the case of unsupervised machine learning where there are no ground truth labels. Although training and testing is possible via the use of numerical simulations (see Sanderson et al. 2020; Ostdiek et al. 2020), such simulations have many limitations themselves and there is no guarantee that the results obtained can be extrapolated to real data sets. Furthermore, the vast majority of clustering algorithms require a selection of parameters which have a deterministic impact on the results (see e.g. Rodriguez et al. 2019, and references therein). At the same time it is very difficult to physically motivate why some parameters should be chosen for a given data set.

In this work we present a data-driven algorithm for clustering in Integrals of Motion space, relying on a minimal set of assumptions. We also derive the statistical significance of each of the structures identified, and define a measure of closeness

between each star in our data set and any of the substructures identified. Our paper is structured as follows: Section 2 describes the construction of our data set and the quality cuts we impose, while Section 3 covers the technical details of the clustering algorithm. In Section 4 we evaluate the statistical significance of the clusters found and present some of their properties, including their structure in velocity space. For each star in our data set we also provide a quantitative estimate that it belongs to any of the statistically significant clusters. The results are interpreted and discussed in Section 5. We also explore here possible relationships between the various extracted clusters and make a comparison to previous work. The first conclusions of our study are summarised in Section 6. In paper II (Ruiz-Lara et al. 2022) we focus on the characterization of the properties of the structures identified in this paper.

## 2. Data

The basis of this work is the *Gaia* EDR3 RVS sample, i.e. stars with line-of-sight velocities measured with the radial velocity spectrometer (RVS) included in the *Gaia* Early Data Release 3 (EDR3, *Gaia* Collaboration et al. 2021), supplemented with radial velocities from ground-based spectroscopic surveys. In particular, we extend the *Gaia* RVS sample with data from LAMOST DR6 low resolution (Wang et al. 2020) and medium resolution (Liu et al. 2019) surveys, RAVE DR6 (Steinmetz et al. 2020b,a), GALAH DR3 (Buder et al. 2021), and APOGEE DR16 (Ahumada et al. 2020). We perform spatial cross-matching between the above mentioned survey catalogues using the TOPCAT/STILTS (Taylor 2005, 2006) `tskymatch2` function. We allow a matching radius between sky coordinates up to 5 arcsec after transforming J2016.0 *Gaia* coordinates to J2000.0, although the average distance between matches is  $\sim 0.15$  arcsec, and 95% are below 0.3 arcsec. For the LAMOST low-resolution survey we apply a +7.9 km/s offset to the measured velocities according to the LAMOST DR6 documentation release<sup>1</sup>. Following Koppelman et al. (2019b), and based on the accuracy of their line-of-sight velocity measurements, we first consider GALAH, then APOGEE, then RAVE, and finally LAMOST while extending the RVS sample. The final extended catalogue contains line-of-sight velocities for 10,629,454 stars with `parallax_over_error` > 5.

In this paper we consider the local halo as stars located within 2.5 kpc, where the distance is computed by inverting the parallaxes after correcting for a zero-point offset of 0.017 mas. We require high-quality parallaxes according to the criterion above, low Renormalised Unit Weight Error (`ruwe` < 1.4) and a maximum error in radial velocity<sup>2</sup> of 20 km/s. We assume  $V_{\text{LSR}} = 232$  km/s, a distance of 8.2 kpc between the Sun and the Galactic Centre (McMillan 2016) and use  $(U_\odot, V_\odot, W_\odot) = (11.1, 12.24, 7.25)$  km/s for the peculiar motion of the sun (Schönrich et al. 2010).

We identify halo stars by demanding  $|\mathbf{V} - \mathbf{V}_{\text{LSR}}| > 210$  km/s, similarly to Koppelman et al. (2018, 2019b). This cut is not too conservative, and will allow for some contamination from the thick disk. Additionally, we remove a small number of stars whose total energy computed using the Galactic gravitational potential described in the next section, is positive. The resulting data set contains  $N = 51671$  sources and we will refer to this selection as the halo set.

<sup>1</sup> <http://dr6.lamost.org/v2/doc/release-note>

<sup>2</sup> This maximum radial velocity error introduces a small bias against very metal-poor stars present in the LAMOST-LRS data set.

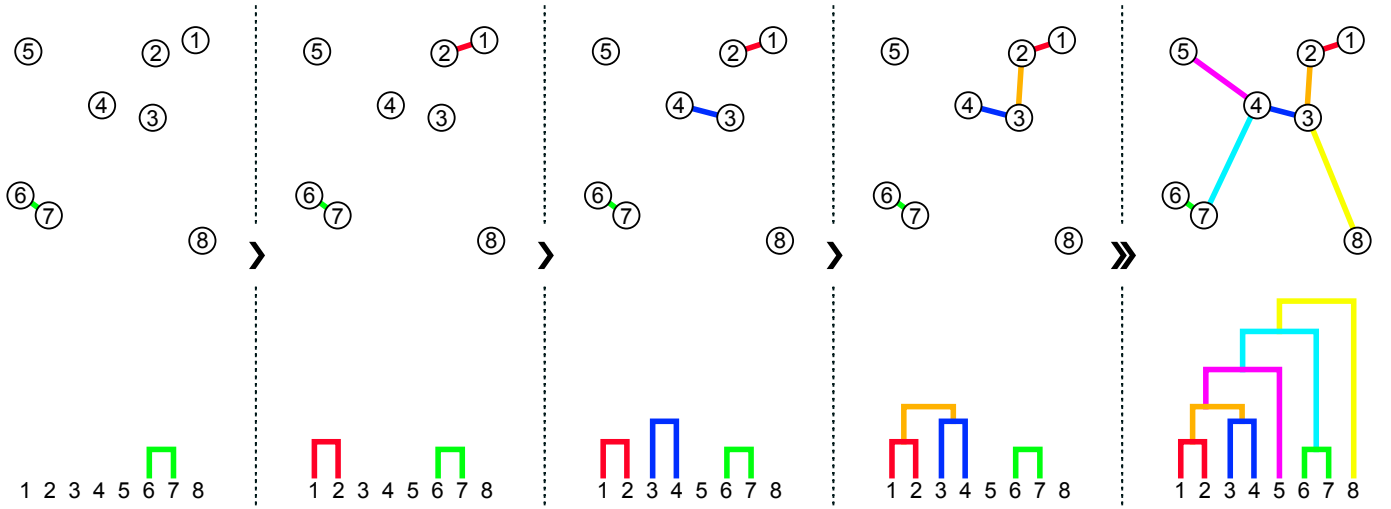


**Fig. 1.** The single linkage algorithm applied on a two-dimensional example. Each step of the algorithm forms a new group by connecting the two closest data points not yet in the same cluster, where each data point is considered a singleton group initially. The resulting merging hierarchy is visualized as a dendrogram at the bottom of each panel.

### 3. Methods

One of the primary goals of this work is to develop a data-driven algorithm, where the extracted structures are statistically based and easily interpretable. At the same time, we want a method that detects more than the most obvious clusters but which ideally is able to scan through the data set without missing any signal.

We use the following notation:  $\mathbf{x}$  for a data point, or star, in our clustering space. The dimensionality of our data-space is denoted by  $n$ ,  $N$  is the number of stars in the data set after applying quality cuts, and as described in Sec. 2 we call this selection the halo set.  $C_i$  denotes a connected component in the halo set, having been formed at step  $i$  of the clustering algorithm. Each  $C_i$  is a candidate cluster for which we want to evaluate the statistical significance. We denote the number of members of a candidate cluster  $N_{C_i}$ .

Note that in this work we consider the data points as such, without taking measurement uncertainties into account. While this would technically be possible, the quality cuts we impose on the data are strict enough to result in reasonably robust outcomes and we leave it to future work to extend the method by taking uncertainties into account in a probabilistic way.

#### 3.1. Clustering algorithm: Single-linkage

While there is a range of clustering algorithms available, what we want is maximum control over the process in combination with an exhaustive extraction of information in the data set. This is especially important as we are dealing with unsupervised machine learning, so from a computational point of view there is no ground truth to verify our findings with.

Our clustering algorithm will have to deal with a potentially large amount of noise in search for significant clusters, which rules out clustering algorithms which assume that all data points belong to a cluster. Some options that can handle noise, and which have also been used for extracting clusters in Integrals of Motion space, would be the Friends-of-Friends algorithm (Efsthathiou et al. 1988), used in e.g. Helmi & de Zeeuw (2000), DBSCAN (Ester et al. 1996), used by Borsato et al. (2020), and HDBSCAN (Campello et al. 2013), as in Koppelman et al. (2019a). The main problem with the former two is that they require spec-

ifying some static parameters, for example a distance threshold for data points of the same cluster. As there is a gradient in density in our halo set (especially, less stars with lower binding energies), using static parameters for this will only work well on some parts of the data space, unless we first apply some advanced non-linear transformations. HDBSCAN is able to extract variable density clusters, but in addition to having a bit of a black box tendency in the application, the output is also dependent on some user-specified parameters. As we want to make as few assumptions as possible about the properties of the clusters, as well as desiring full control over the clustering process, we consider a simpler option.

The single linkage algorithm is a hierarchical clustering method which only requires a selection of distance metric (Everitt et al. 2011). We use standard Euclidean distance to this end. At each step of the algorithm it connects the two groups with the smallest distance between each other, defined as the smallest distance between two data points not yet in the same group, where each data point is considered a singleton group initially. Each merge, or step  $i$  of the algorithm, corresponds to a new connected component in the data set. This is illustrated in Fig. 1. Here we see single linkage applied on a two-dimensional example, where the top part of each panel illustrates the merging process of the algorithm and in the bottom we illustrate the resulting merging hierarchy in a dendrogram. If the data set is of size  $N$  the algorithm will perform  $N - 1$  steps in total, as it keeps going until the full data set has been linked. Hence, the algorithm is also closely related to graph theory, as the result after the last merge is equivalent to the minimum spanning tree (Gower & Ross 1969). Correspondingly - from a computational point of view - the series of connected components obtained also corresponds to the set of every potential cluster in the data, under the assumption that the most likely clusters are the groups of data points with the smallest distance between each other, without assuming any specific cluster shape.

The core idea of our clustering method is to apply the single linkage algorithm to the halo set and subsequently evaluate each connected component (or candidate cluster  $C_i$ , formed at step  $i$  of the algorithm) by a cluster quality criterion. The clusters that exhibit statistical significance according to the selected criterion are accepted. This way the method will also be able to

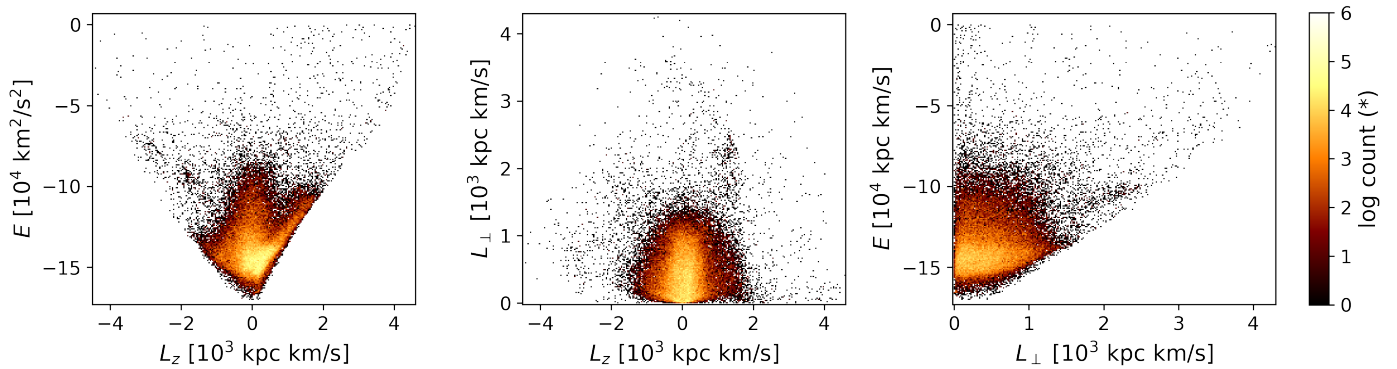


**Fig. 2.** Distribution of stars in our halo sample in Integrals of Motion space. The single-linkage algorithm identifies clusters in the 3D space resulting from the combination of our three clustering features, namely energy  $E$ , and two components of the angular momentum  $L_z$  and  $L_\perp$ .

handle noise, as the data points that do not belong to any cluster displaying a high statistical significance will be discarded.

### 3.2. Clustering in Integrals of Motion space

As described earlier, to identify merger debris we will be relying on the expectation that it should be clustered in Integrals of Motion space. As Integrals of Motion we use three typical quantities: The angular momentum in  $z$ -direction  $L_z$ , the perpendicular component of the total angular momentum vector  $L_\perp$ , and total energy  $E$ . While  $L_z$  is truly conserved in an axisymmetric potential,  $L_\perp$  typically varies slowly retaining a certain amount of clustering for stars on similar orbits, as those originating in the same accretion event, although not being fully conserved. The total energy  $E$  is computed as

$$E = \frac{1}{2}v^2 + \Phi(\mathbf{r}) \quad (1)$$

where  $\Phi(\mathbf{r})$  is the Galactic gravitational potential at the location of the star. For this we use the same potential as in Koppelman et al. (2019b): A Miyamoto-Nagai disk, Hernquist bulge, and Navarro-Frank-White halo with parameters  $(a_d, b_d) = (6.5, 0.26)$  kpc,  $M_d = 9.3 \times 10^{10} M_\odot$  for the disk,  $c_b = 0.7$  kpc,  $M_b = 3.0 \times 10^{10} M_\odot$  for the bulge, and  $r_s = 21.5$  kpc,  $c_h = 12$ , and  $M_{\text{halo}} = 10^{12} M_\odot$  for the halo. While the choice of potential influences the absolute values we compute for total energy, the difference in the distributions of data points between two reasonably realistic potentials is negligible in the clustering space, as shown in Section 5.

We scale each of the Integrals of Motion or “features” linearly to the range  $[-1, 1]$  using a set reference range of  $E = [-170000, 0]$  km<sup>2</sup>/s<sup>2</sup>,  $L_\perp = [0, 4300]$  kpc km/s, and  $L_z = [-4500, 4600]$  kpc km/s, roughly corresponding to the minimum and maximum values in the halo set. Our equal range scaling also implies that each of the three features is considered equally important in a distance-based clustering algorithm. The halo set visualized for all combinations of the clustering features can be seen in Fig. 2.

### 3.3. Random data sets

To assess the statistical significance of the outcome of our clustering algorithm, we will be using random data sets. To this end, we create a reference halo set using our existing data set, but recompute the Integrals of Motion using random permutations of the  $v_y$  and  $v_z$  components, similarly to Helmi et al. (2017). This

creates an artificial data set which has similar properties to the observed data, but where the correlations in the velocity components and hence structure in Integrals of Motion space is broken up. Specifically, we scramble the velocity components of all stars with  $|\mathbf{V} - \mathbf{V}_{\text{LSR}}| > 180$  km/s (so a slightly more relaxed definition of the halo, comprising 75149 sources of our original data set). The majority of these stars with scrambled velocities will satisfy the criterion we use to kinematically define halo stars,  $|\mathbf{V} - \mathbf{V}_{\text{LSR}}| > 210$  km/s, thus for each artificial halo we sample  $N$  stars satisfying the above mentioned criterion and recompute the clustering features, where  $N$  is the number of stars in our original halo set. We normalize these features with the same scaling as for the original halo set, such that the mapping from absolute to scaled values is identical for the real and artificial data.

We generate  $N_{\text{art}} = 100$  realisations of this artificial halo as reference. An example artificial data set is displayed in Fig. 3, where an arbitrarily chosen realization is visualized. Comparing to Fig. 2 we see that the two data sets have very similar characteristics, but that the by eye visible substructure in the original halo set has been diluted.

## 4. Results

### 4.1. Identification of clusters

We apply the algorithm described above on our halo set. For computational efficiency we only investigate candidate clusters having at least 10, and less than 25000 data points (48% of the data set). The former is the smallest group that would be statistically significant assuming Poissonian statistics together with the significance level we adopt, while the latter assumes that no accreted structure should dominate a larger fraction of the local halo than this. This limit is justified by recent work indicating that  $\sim 40 - 50\%$  of the stars in the halo near the Sun were born in-situ and are part of a hot thick disk (see e.g. Helmi 2020).

#### 4.1.1. Evaluating statistical significance

In order to examine the quality of each candidate cluster obtained by the linking process, we need a cluster evaluation metric. A challenge is that our three-dimensional clustering space has a higher density of stars with low energy and angular momentum than regions with higher energy, as seen in Fig. 2. Therefore we will be using our randomized data sets to compare the observed and the expected density for different regions. We will thus examine the candidate clusters resulting from applying the single linkage algorithm and assess their statistical significance

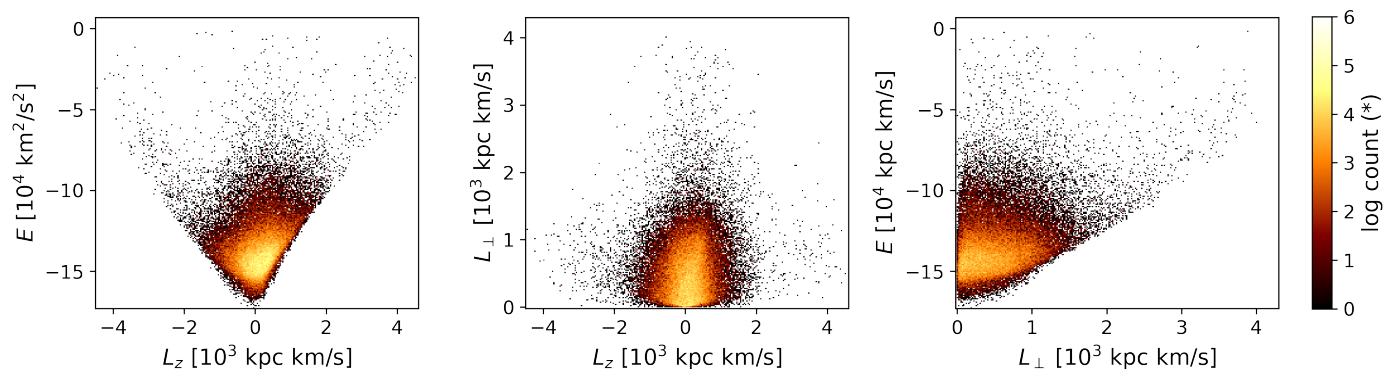


**Fig. 3.** Example of the distribution of points in Integrals of Motion for one of the random halo sets (# 1 out of  $N_{\text{art}} = 100$ ) obtained by re-shuffling of the velocity components. See for comparison Fig. 2.

by computing the expected density of stars in a region, and comparing the difference between the observed and expected count in relationship to the statistical error on these quantities.

In order to compare the number of members of a candidate cluster  $C_i$  to the expected count (obtained from our randomized sets), we need to determine the region in which  $C_i$  resides. To this end, we define an ellipsoidal boundary around  $C_i$  by applying Principal Component Analysis (PCA) on the members. The standard equation of an  $n$ -dimensional ellipsoid centered around the origin is

$$\sum_{i=1}^n \frac{x_i^2}{a_i^2} = 1 \quad (2)$$

where  $a_i$  denotes the length of each axis. The variance along each principal component of the cluster is given by the eigenvalues  $\lambda_i$  of the covariance matrix and we can define the length of each axis  $a_i$  of the ellipsoid in terms of the number of standard deviations of spread along the corresponding axis. We consult the  $\chi^2$  distribution with three degrees of freedom (corresponding to our three-dimensional clustering space) and observe that 95.4% of a three-dimensional Gaussian distribution falls within 2.83 standard deviations of extent along each axis. This is the fraction of a distribution corresponding directly to a two standard deviation axis length in 1D. Hence, we choose the axis lengths to be  $a_i = 2.83 \sqrt{\lambda_i}$ . The choice to cover 95.4% of the distribution provides a snug boundary around the data points that is neither too strict nor includes too much empty space.

Now we can compute the number of stars falling within the ellipsoidal cluster boundary by analysing the PCA-transformation of  $C_i$  and mapping the stars of the data sets to the PCA-space defined by  $C_i$  by subtracting the means and multiplying each data point by the eigenvectors of the covariance matrix. Hereby we obtain a mean-centered and rotated version of the data where the direction of maximum variance aligns with the axis of the coordinate system.

We compute both the average number of stars from the artificial halo  $\langle N_{C_i}^{\text{art}} \rangle$  and number of stars from the real halo set  $N_{C_i}$  that fall within this boundary. The statistical significance of a cluster is then obtained by the difference between the observed and expected count, divided by the statistical error on both quantities. In this work we demand a minimum significance level of  $3\sigma$ , defined by

$$N_{C_i} - \langle N_{C_i}^{\text{art}} \rangle > 3\sigma_i, \quad (3)$$

and where  $\sigma_i = \sqrt{N_{C_i} + (\sigma_{C_i}^{\text{art}})^2}$ . Here  $\sigma_{C_i}^{\text{art}}$  is the standard deviation in the number counts across our 100 artificial halos. We

treat the observed data as having Poissonian properties, giving the statistical error on the observed cluster count as  $\sqrt{N_{C_i}}$ .

#### 4.1.2. Statistically significant groups

Evaluating the statistical significance for all candidate clusters returned by the single linkage algorithm gives us a set of clusters having at least a  $3\sigma$  significance, where some are hierarchically overlapping subsets of each other. A structure is likely to display statistical significance starting from the core of the cluster, growing out to its full extent via a series of merges in the algorithm, each being deemed statistically significant. Similarly a cluster with a dense core together with some neighbouring noise will still display significance if the core is dense enough.

Under the hypothesis that the statistical significance increases while more stars of the same structure are being merged into the cluster, and that the significance decreases when noise in the outskirts is added, final (exclusive) cluster labels are found by traversing the merging tree of the overlapping significant clusters and picking the location where they reach their maximum significance. In practice this is done by iterating over the clusters ordered by descending significance, traversing its parent clusters upwards in the tree, and selecting the location where the maximum significance is reached. Nodes higher up in the merging hierarchy than the maximum significance for this path are removed, as we do not want a path with a smaller maximum significance to override the selection by deeming a larger cluster on the same path to be a final cluster.

After finding a cluster in the tree at its maximum significance, we assign the same label to all stars that belong to this connected component according to the single linkage algorithm. Conveniently, if we choose a lower significance level than  $3\sigma$ , the change will simply extract additional clusters of a lower significance that will not overlap with those of higher significance.

The results of the methodology described above are shown in Fig. 4 which plots the distribution of the individual clusters identified for the various subspaces (top panel) and in velocity space (bottom panel). The colors here are for illustration purposes only and there are enough clusters such that some of them are plotted in very similar nuances.

One of clusters identified by the single-linkage algorithm (assigned label or cluster ID #1) is the globular cluster M4 - the lowest energy cluster extracted, seen in dark blue in the top left panel of Fig. 4. Although all of its associated stars have nominally good parallax estimates, a subset of these have rather large correlation values in the covariance matrix provided by



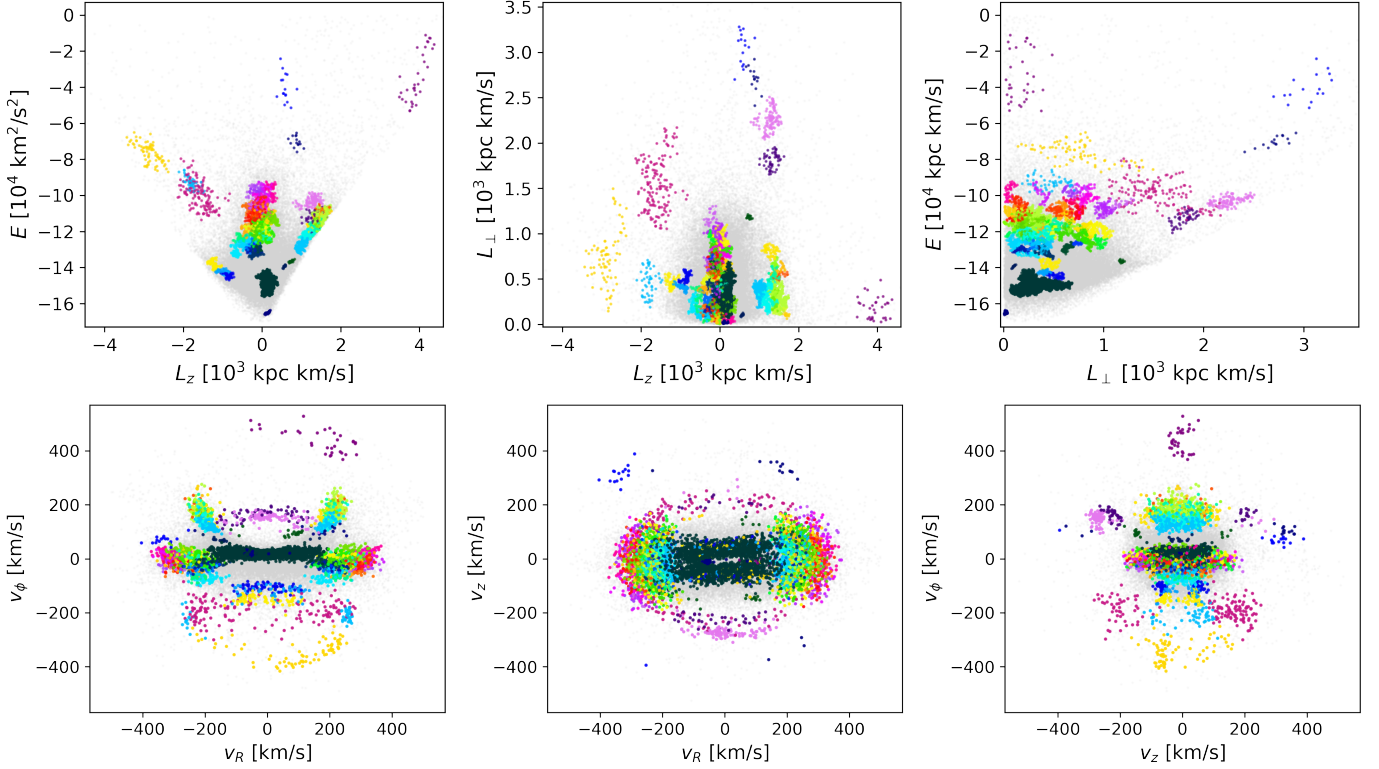


**Fig. 4.** Clusters extracted by the algorithm, visualized in Integrals of motion (top row) and in velocity space (bottom row). The different colors indicate the stars associated to the 67 different clusters identified.

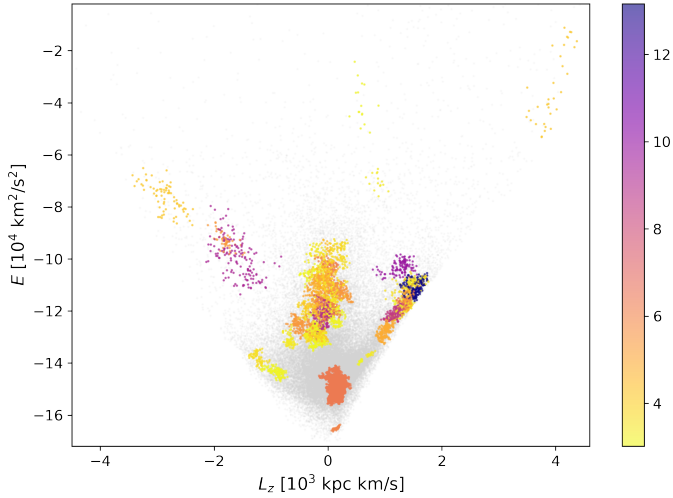


**Fig. 5.** Distribution of the 67 high-significance clusters in the  $E - L_z$  plane, color-coded according to their statistical significance.

the *Gaia* database, particularly for terms involving the parallax (explaining finger-of-god features in velocity space). This finding prompted us to inspect all of the significant clusters, and we noticed that also cluster #67 has members depicting similarly large values of correlation terms involving parallax (namely those with declination and  $\mu_\delta$ , in particular, most of its stars either have `dec_parallax_corr` that is below -0.15 or `parallax_pmdec_corr` above 0.15). These stars are also located towards the Galactic centre and anticentre, thus also in relatively crowded regions. Cluster #67 stars' average value

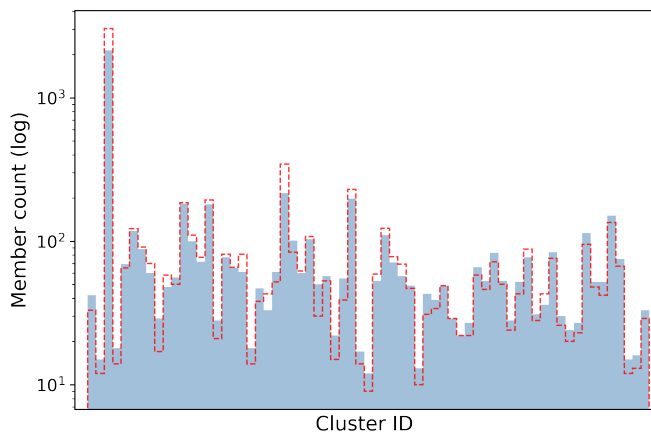
in `dec_parallax_corr` and `parallax_pmdec_corr` is significantly worse than any other cluster, resulting in an average `parallax_err`=0.1, compared to an average value smaller than 0.045 for all other clusters. To avoid confusion, we have not plotted this cluster in Figure 4 and do not consider it further in our analysis.

Figure 5 shows the clusters color-coded by their statistical significance. The algorithm has identified 67 clusters with a total of 6209 stars assigned to them, with the range in significance values being [3.0, 13.2]. The figure shows that those clusters with the highest significance are located in regions of already known substructures, such as for example the Helmi Streams near  $L_z \sim 1500 \text{ kpc km/s}$  and  $E \sim -10^5 \text{ km}^2/\text{s}^2$  (Helmi et al. 1999; Koppelman et al. 2019b).

In Fig. 6 we show the distribution of the number of members of the clusters identified by our procedure, plotted as the histogram with blue bars. The median number of stars in a cluster is 53, while the largest cluster has 2137 stars associated. These numbers reflect the members identified by the linking process, belonging to some significant cluster  $C_i$ . For most clusters, it is possible to identify additional plausible members following a procedure described in Sec. 4.3. The resulting cluster sizes are shown as the red dashed histogram in Fig. 6.

#### 4.2. Extracting subgroups in velocity space

The velocity distributions of the extracted clusters can give us more clues about their validity and properties, since an accreted structure observed within a local volume is expected to display (sub)clumping in velocity space, representing debris streams with different orbital phases.



**Fig. 6.** Histogram of the number of members per cluster, with members identified by the single linkage algorithm plotted in solid blue. The dashed red line indicates the sizes when original and additional plausible members are considered within a Mahalanobis distance of  $D_{\text{cut}} \sim 2.13$  from each cluster centre.

We extract these subgroups in velocity space by applying another round of clustering on each of the 67 clusters. As the data set representing such a cluster in velocity space is far smaller and less complex than our original halo set, and the subgroups in velocity space are often clearly separated clumps, we simply apply the HDBSCAN algorithm (Campello et al. 2013). This is a robust clustering algorithm which is capable of extracting variable density clusters, as well as labelling possible noise, while being able to handle various cluster shapes.

We apply HDBSCAN directly to the  $v_R$ ,  $v_\phi$  and  $v_z$  components of each cluster, without scaling, as the range for these values are already of the same magnitude. We set the parameter `min_cluster_size` (smallest group of data points that the algorithm will accept as an entity) to 5% of the cluster size, with a lower limit of 3 stars. We assign `min_samples` = 1, regulating how likely the algorithm is to classify an outlier as noise, with a smaller value being less strict. The default mode of HDBSCAN does not allow for a single cluster to be returned, as its excess of mass algorithm may bias towards the root node of the data hierarchy. Since it is not unlikely that a single-linkage cluster could correspond to a single group in velocity space but this will not always be the case, we circumvent this issue by setting the parameter `allow_single_cluster` to `True` only if the standard deviation in  $v_R$ ,  $v_\phi$  and  $v_z$  is small (below 30 km/s), for at least two out of the three velocity directions. The idea is that if a cluster seems to be a single subgroup, it might display an elongated dispersion along at most one of these components, but if the dispersion is large for two or more out of the three, the cluster is likely to contain at least two kinematic subgroups.

In this way, the HDBSCAN algorithm extracts 232 subgroups where the number of subgroups per cluster varies in the range [1, 12], with the mean and median being 3.5 and 3 respectively. This is likely a lower limit to the true number of subgroups in velocity space, particularly because of the limitation in the number of stars, which prevent us from detecting streams with fewer than 3 stars in the data set, but also due to the difficulty with defining optimal parameters for clustering in this space.

A series of examples of the output of HDBSCAN are displayed in Fig. 7. Here each row reflects one cluster with the first three panels displaying the projection of the subgroups in velocity space, and the rightmost panel displaying the location of the

cluster in  $E - L_z$  space with the cluster ID indicated in the top right corner. Non-members are plotted in grey, and noise as labelled by HDBSCAN with black open circles. The subgroups we find in velocity space for the statistically significant clusters are often quite distinct, for example in the case of clusters #3, #56 and #60. Cluster #3 is an example of a cluster which would be classified as a single subgroup in case the parameter `allow_single_cluster` would be statically `True`, demonstrating the necessity of our approach. Cluster #64 is split into three subgroups, even though it could possibly be divided into either two or four groups as well. Cluster #64 is the cluster with the largest number of subgroups, being divided into twelve small portions.

We can also look at the dispersion in the velocity components of these subgroups to characterize them further. This is computed by applying PCA on the  $v_x$ ,  $v_y$  and  $v_z$  components of each subgroup with at least 10 members (107 in total), and measuring the standard deviation along the resulting principal components. A histogram of these dispersions is displayed in Fig. 8. There are 11 subgroups with a dispersion in the third principal component smaller than 10 km/s, and three below 5 km/s. The smallest value of 2.5 km/s is associated with the globular cluster M4 (cluster #1) and the second smallest (4.4 km/s) with cluster #64, which can be seen as the yellow subgroup in the corresponding panel in Figure 7.

The distribution of the 3D velocity dispersion  $\sigma_{\text{tot}}$  of the subgroups can be seen in the bottom panel in Fig. 8, where the smallest value again is for the globular cluster M4. A single subgroup, being the green subgroup of cluster #63 in Fig. 7, is truncated from Fig. 8 as it has a total velocity dispersion of 186 km/s.

#### 4.3. Evaluating proximity of stars to clusters

Now that we have obtained our cluster catalogue, we would like to obtain estimates for the likelihood of any individual star to belong to some specific cluster. This is done both in order to identify possible new members of a cluster, as well as to find the most likely members e.g. for observational follow-up.

We do this by describing each cluster in Integrals of Motion space as a Gaussian probability density, defined by the mean and covariance matrix of the associated stars identified by the single-linkage algorithm. The idea is that the core of the over-density will be located around the mean of the Gaussian, and less likely members will be located in the outskirts of the distribution. We can then compute where a data point  $\mathbf{x}$  is located within the Gaussian distribution by calculating its Mahalanobis distance  $D$

$$D = \sqrt{(\mathbf{x} - \boldsymbol{\mu})^T \boldsymbol{\Sigma}^{-1} (\mathbf{x} - \boldsymbol{\mu})} \quad (4)$$

where  $\boldsymbol{\mu}$  is the mean of the cluster distribution and  $\boldsymbol{\Sigma}^{-1}$  is the inverse of the covariance matrix. Therefore, the Mahalanobis distance expresses the distance between a data point and a Gaussian distribution in terms of standard deviations after that the distribution has been normalized to unit spherical covariance.

The theoretical distribution of squared Mahalanobis distances of an  $n$ -dimensional Gaussian is known: it is the  $\chi^2$  distribution with  $n$  degrees of freedom. Fig. 9 shows the distribution of Mahalanobis distances for the stars assigned to clusters by our procedure, compared to the  $\chi^2$  with  $n = 3$  degrees of freedom. This figure demonstrates that the distribution of the members of the clusters is somewhat similarly to a multivariate Gaussian, but that this is slightly more peaked in comparison to what is seen for the cluster members.

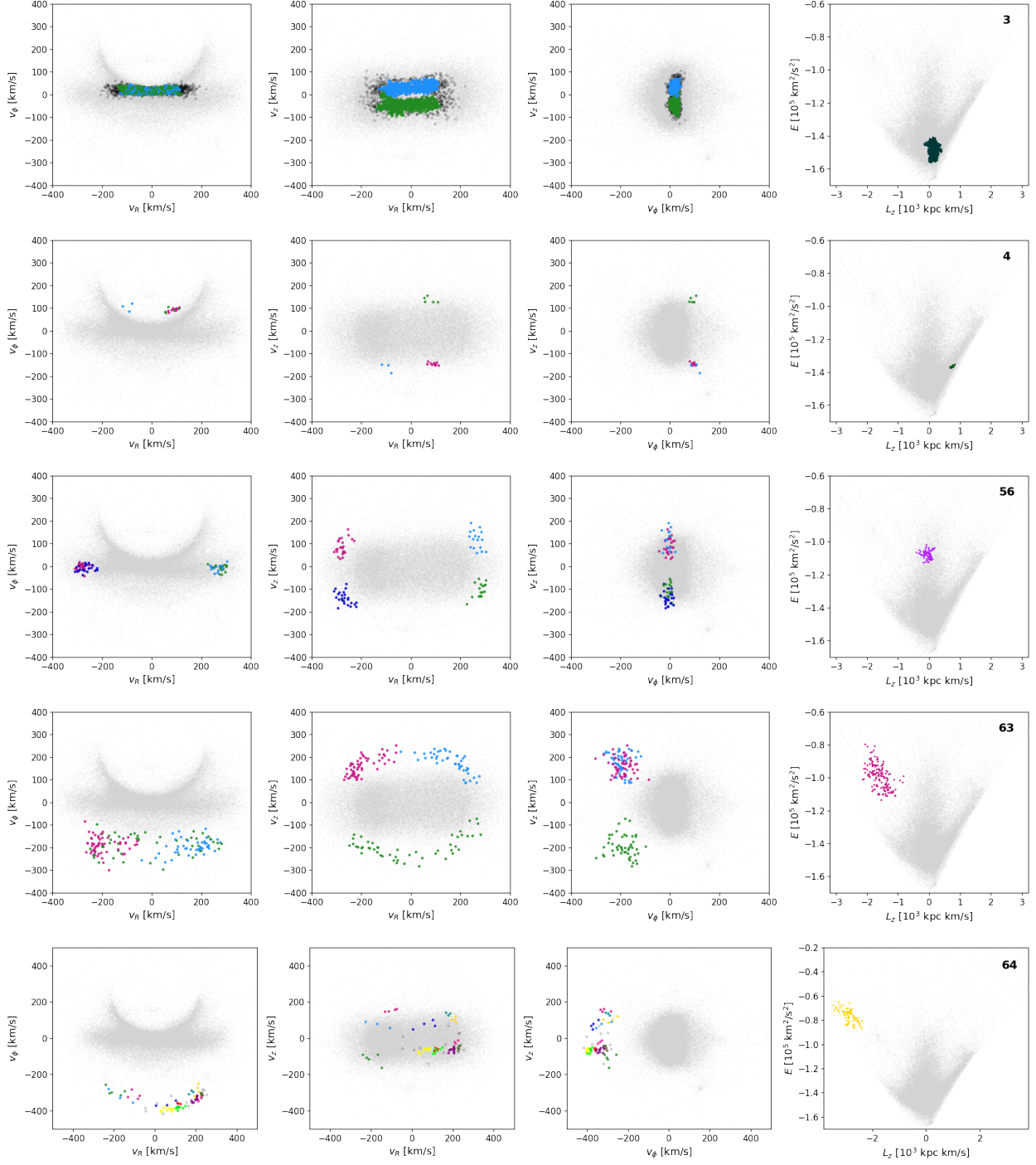


**Fig. 7.** Subgroups identified by HDBSCAN in velocity space for a selection of 5 significant clusters from the single-linkage algorithm, where noise as labelled by the algorithm is marked with open black circles. In each row, the three first panels display the projection of the subgroups in velocity space and the fourth panel the location of the “parent” cluster in  $E - L_z$  space, with its ID displayed in the upper right corner.

We can thus use the Mahalanobis distance of each star to refine the detected clusters, select core members and identify additional plausible members. To establish what is a meaningful value of the Mahalanobis distance  $D_{\text{cut}}$ , we proceed as follows. We investigate the internal properties of the clusters as defined by the algorithm, as well as by considering only those stars within different values of  $D_{\text{cut}}$  (corresponding to the 50<sup>th</sup>, 65<sup>th</sup>, 80<sup>th</sup>, 90<sup>th</sup>, 95<sup>th</sup>, and 99<sup>th</sup> percentiles of the distribution of original members, see Fig. 9). Specifically, we check the distribution of stars in the Colour-absolute Magnitude Diagrams and the metal-

licity distribution functions for each cluster. We find that a too restrictive cut (50<sup>th</sup>, 65<sup>th</sup> percentiles) reduces the number of stars in a way that often limits the characterization of the properties of the clusters. A too loose cut (95<sup>th</sup>, 99<sup>th</sup> percentiles), although greatly increasing the number of stars in clusters, leads to a noticeable amount of contamination, hence affecting the properties of the clusters. As a compromise between a manageable amount of contamination and increase in purity of the clusters as well as in number of stars, we decide to use the 80<sup>th</sup> percentile cut, corresponding to a Mahalanobis distance of  $D_{\text{cut}} \sim 2.13$ .



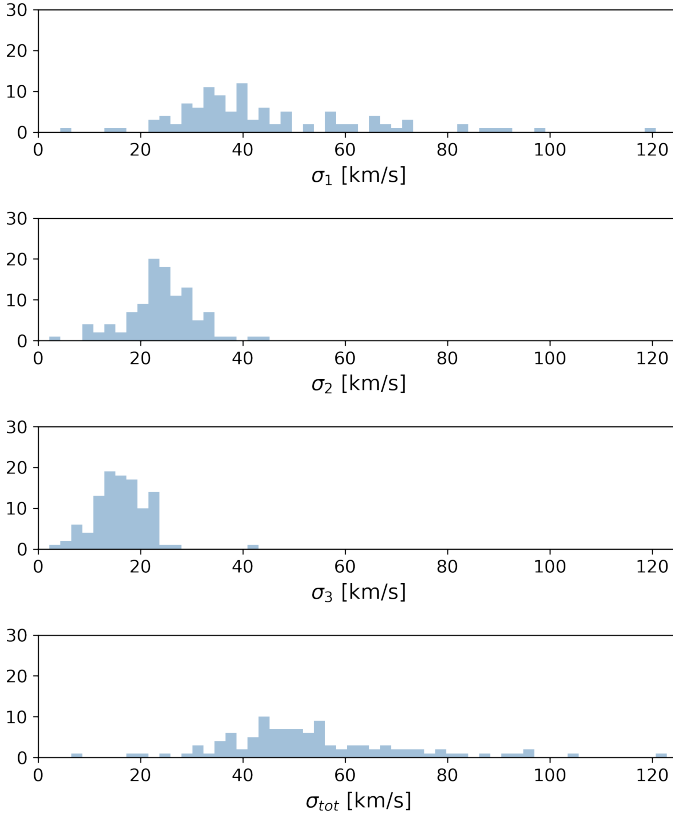


**Fig. 8.** Velocity dispersions of each subgroup with at least 10 members identified by HDBSCAN, computed along the principal axes (top three panels), and the total 3D value (bottom panel).

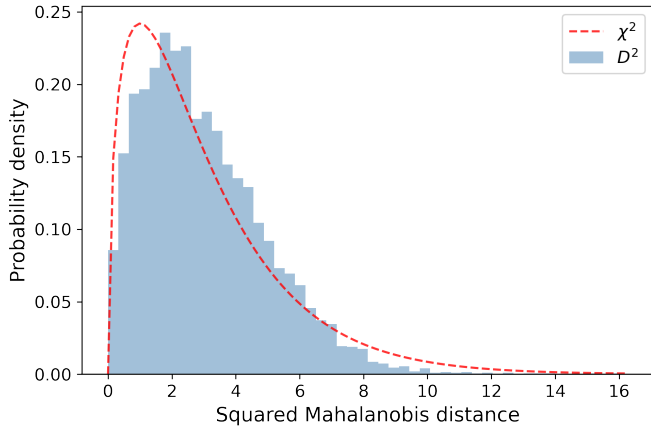


**Fig. 9.** Distribution of squared Mahalanobis distances of the stars assigned to a cluster versus the chi-square distribution with three degrees of freedom.

Out of the stars in our halo set that have not yet been given a label, we can associate 2104 additional stars to one of the clusters on the basis of the star being within a Mahalanobis distance of 2.13 to its closest cluster. There are 1186 original members falling outside of the Mahalanobis distance cut. There are 7127 stars in total in the halo set (13.8%) that are within  $D_{\text{cut}} = 2.13$  of some cluster.

The histogram of the number of cluster members contained within  $D_{\text{cut}}$  is displayed in Fig. 6 as the red dashed line. The largest cluster #3 has 3032 such members, while the smallest

is #34 with such 9 members. The mean and median sizes of the clusters after the identification of additional members within  $D_{\text{cut}}$  become 106 and 49 respectively.

Table 1 lists the clusters identified, their statistical significance ( $\sigma_i$ ), number of members indicated by the clustering ( $N_{\text{orig}}$ ) and with additional members ( $N_{\text{tot}}$ ), the centroid ( $\mu$ ) and entries of covariance matrix ( $\sigma_{ij}$ ). To transform the values listed in the table to the corresponding physical quantities, for the means we can use that

$$\langle \mu_i \rangle f = \frac{2}{\Delta_i} (\langle I_i \rangle - I_{i,\min}) - 1$$

where  $f = 10^{-3}$  and  $\Delta_i = I_{i,\max} - I_{i,\min}$ , with  $i = 0..2$  and  $I_i$  corresponding to  $E$ ,  $L_{\perp}$  and  $L_z$  respectively, with the minimum and maximum values given in Sec. 3.2. For the covariance matrix, these definitions lead to

$$\sigma_{ij} f^2 = \frac{4}{\Delta_i \Delta_j} \Sigma_{I_{i,j}}$$

where  $\Sigma_{I_{i,j}}$  is the covariance matrix in Integrals of Motion-space. Table 2 lists for the stars in our halo set, their kinematic and dynamical properties, as well as the cluster to which they were associated to by the single-linkage algorithm, and that to which they are associated on the basis of their Mahalanobis distance, which is also listed to help assess membership probability. Both tables are available in their entirety online.

## 5. Discussion

Given the relatively large number of clusters identified it is important to understand how they relate to each other. We explore their internal hierarchy in our clustering space using the Mahalanobis distance between two distributions

$$D' = \sqrt{(\mu_1 - \mu_2)^T (\Sigma_1 + \Sigma_2)^{-1} (\mu_1 - \mu_2)} \quad (5)$$

where  $\mu_1, \mu_2$  and  $\Sigma_1, \Sigma_2$  describe the means and covariance matrices of the two cluster distributions, respectively, and  $D'$  gives a relative measure of their degree of overlap. A dendrogram of the clusters according to single linkage by Mahalanobis distance can be seen in Fig. 10.

### 5.1. How many independent clusters?

An initial inspection of the dendrogram shown in Fig. 10 reveals a complex web of relationships between the significant clusters extracted by our single linkage algorithm. Some of these clusters are linked to others only at large distances (namely clusters #1, #2, #3, #4, or #68), whereas others are clearly grouped together, sometimes even in a hierarchy of substructures. This suggests that the 67 clusters that our methodology identified as significant are not fully independent from each other.

As a first attempt to explore the hierarchy we observe in the dendrogram, we tentatively set a limit at Mahalanobis distance  $\sim 4.0$  (horizontal dashed line in Fig. 10). This Mahalanobis distance is large enough such that not all 67 clusters are considered individually, but also small enough that at least some substructures already reported in the literature can be distinguished (see for instance Koppelman et al. 2019a; Naidu et al. 2020). According to this experimental limit, we may tentatively identify 6 different large substructures (colour-coded in Fig. 10), as well as a few independent clusters. The distribution of these substructures in the  $E - L_z$  plane is displayed in Fig. 11. This figure shows

**Table 1.** Overview of the characteristics of the extracted clusters, where their significance is listed, the number of members as determined by the single linkage ( $N_{\text{orig}}$ ) and in total after considering members within a Mahalanobis distance of 2.13 ( $N_{\text{Dcut}}$ ).  $\mu$  is the centroid of the scaled clustering features as determined by the original members, and  $\sigma_{ij}$  represents the corresponding entries in the covariance matrix. The indices 0-3 correspond to the order  $E$ ,  $L_{\perp}$  and  $L_z$ . The full table will be made available online.

Label	signif.	$N_{\text{orig}}$	$N_{\text{Dcut}}$	$\mu_0 [10^{-3}]$	$\mu_1 [10^{-3}]$	$\mu_2 [10^{-3}]$
1	6.0	42	33	-941.5	-989	22
2	3.1	15	12	-640.1	-952	114
3	6.3	2137	3032	-759.6	-851	24
4	3.3	18	14	-607.4	-450	152
5	4.1	69	65	-519.7	-703	-38
6	3.0	118	122	-546.2	-809	-47
7	3.8	88	91	-533.0	-914	-60
8	3.1	60	70	-699.6	-757	-201
9	3.1	29	17	-488.2	-659	-51
10	3.1	48	58	-505.8	-869	-83
$\sigma_{00} [10^{-6}]$	$\sigma_{01} [10^{-6}]$	$\sigma_{02} [10^{-6}]$	$\sigma_{11} [10^{-6}]$	$\sigma_{12} [10^{-6}]$	$\sigma_{22} [10^{-6}]$	
50.7	6.3	52.7	21.0	9.2	76.9	
57.6	37.8	30.7	28.5	19.1	25.8	
1324.0	255.9	23.2	3916.6	210.6	369.2	
42.9	-11.3	44.0	49.1	-19.2	81.3	
276.8	157.7	-63.5	221.7	-63.7	179.5	
433.2	-252.2	102.0	484.5	-133.5	311.3	
136.6	-49.0	-51.0	410.1	231.0	418.6	
179.0	-139.4	-79.4	484.1	168.0	296.1	
63.4	24.2	-37.9	160.9	-76.5	214.2	
648.9	31.8	216.3	241.8	-65.5	162.4	

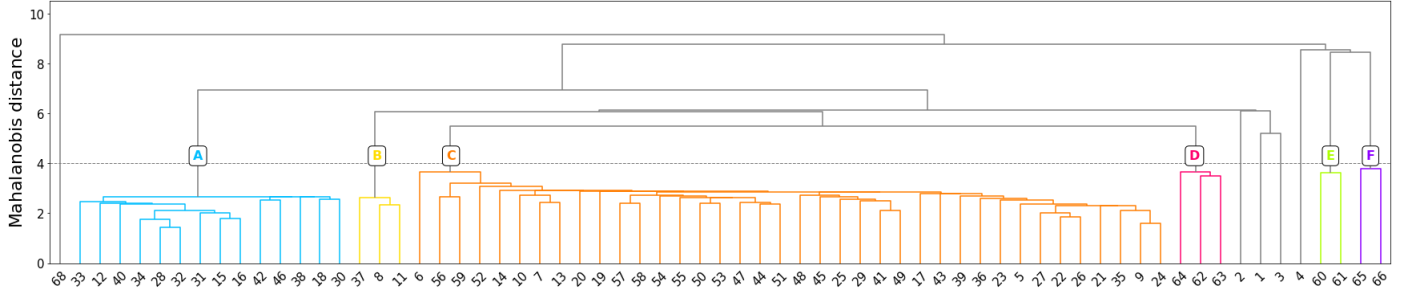


**Fig. 10.** Relationship between the significant clusters according to the single linkage algorithm, obtained using the Mahalanobis distance in the clustering space.

that some of these groups do indeed correspond to previously identified halo substructures (see also Sec. 5.2).

The rich substructure found by the single linkage algorithm within each of these tentative groups deserves further inspection. For instance, the large group labeled as ‘C’ in Fig. 10, which according to its location in the  $E - L_z$  plane could correspond to *Gaia*-Enceladus (Helmi et al. 2018), can be clearly split in several subgroups according to the dendrogram. In addition, there are some individual clusters such as cluster #6 linking at large Mahalanobis distances that could potentially be considered as part of *Gaia*-Enceladus. Similarly, clusters belonging to the light blue branch (substructure B), that falls in the region in  $E - L_z$  occupied by Thamnos (Koppelman et al. 2019a), also shows different clustering levels, with cluster #37 being linked at a larger Mahalanobis distance than clusters #8 and #11.

To fully assess the tentative division of our halo set into 6 main groups, as well as to study the significance and independence of the finer structures within the groups, would require a detailed analysis of the internal properties of these clusters and substructures, such as their stellar populations, metallicities, and chemical abundances. We defer such an exhaustive analysis to

a separate paper (Ruiz-Lara et al. 2022). Nonetheless, as a first example, we here focus our attention on the pair of clusters #60 and #61, identified as substructure E, that are likely part of the Helmi streams (Helmi et al. 1999).

These two clusters are directly linked according to the dendrogram in Fig. 10. The middle and right-hand panels of Fig. 12 show the colour-absolute magnitude diagram (CaMD<sup>3</sup>) and the metallicity distribution functions (from the LAMOST-LRS survey) for both clusters. These figures demonstrate that indeed, the clusters’ stars depict similar distributions in the CaMD, with ages older than  $\sim 10$  Gyr, and metallicities drawn from the same distribution, having a Kolmogorov-Smirnov statistical test p-value of 0.99. All this evidence supports a common origin for both clumps as debris from the Helmi streams.

The separation of the Helmi streams in two significant clusters in Integrals of Motion space is in agreement with the recent findings presented in Dodd et al. (2021). In this work, the authors establish that the two clumps, which are clearly split in an

<sup>3</sup> We correct for reddening using the dust map from Lallement et al. (2018) and the recipes to transform to *Gaia* magnitudes given in *Gaia* Collaboration et al. (2018a)

**Table 2.** Overview of fields in our final star catalogue. It contains *Gaia* source ids, heliocentric Cartesian coordinates, heliocentric Cartesian velocities, and the four features used for clustering. The column significance indicates significance of the cluster a star belongs to,  $\text{Label}_{\text{orig}}$  the label of the cluster according to the single linkage process,  $\text{Label}_{D_{\text{cut}}}$  is the cluster label after selecting the cluster with the smallest Mahalanobis distance  $D$  (requiring at least  $D < 2.13$ ). The full table will be made available online.

source_id	$x$	$y$	$z$	$v_x$ [km/s]	$v_y$ [km/s]	$v_z$ [km/s]
494990686553088	-0.82	0.07	-0.92	-252.3	-249.5	29.7
2131751183780736	-0.52	0.07	-0.54	-262.9	-247.3	45.4
2412092288843648	-0.12	0.01	-0.12	-105.8	-210.9	-51.9
4032119593003520	-1.56	0.17	-1.49	220.9	-239.3	72.0
4564455019620096	-0.58	0.09	-0.66	-204.4	-83.7	57.1
4641558272441088	-0.65	0.11	-0.74	13.8	-91.5	-283.0
5201244050756096	-0.76	0.12	-0.81	127.5	-120.1	-201.5
5366583111858688	-0.41	0.07	-0.45	169.9	-108.1	-93.3
6932768706211328	-1.58	0.22	-1.55	176.6	-253.7	99.5
7299795136273664	-0.74	0.13	-0.72	273.0	-256.0	95.1
$E$ [ $10^5 \text{ km}^2/\text{s}^2$ ]	$L_{\perp}$ [ $10^3 \text{ kpc km/s}$ ]	$L_z$ [ $10^3 \text{ kpc km/s}$ ]	significance	$\text{Label}_{\text{orig}}$	$\text{Label}_{D_{\text{cut}}}$	$D$
-1.192	0.56	-0.06	8.9	24	24	1.43
-1.184	0.60	-0.04	8.9	24	24	1.16
-1.485	0.36	0.28	6.3	3	3	1.46
-1.141e	0.43	0.10	5.5	26	0	2.27
-1.172	0.70	1.40	3.4	30	30	1.34
-1.002	2.46	1.36	9.8	60	60	1.79
-1.133	1.85	1.14	3.6	61	61	1.76
-1.228	0.83	1.19	3.1	38	38	1.61
-1.206	0.75	-0.04	8.9	24	24	0.83
-1.042	0.71	-0.06	3.6	51	51	1.63

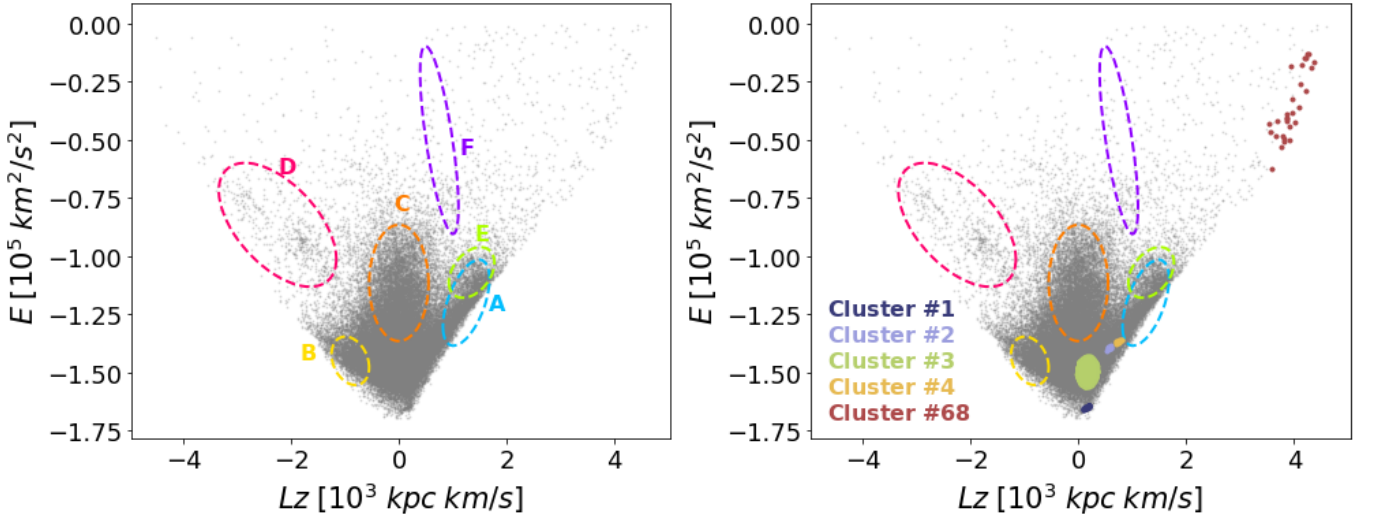


**Fig. 11.** Location in the  $E - L_z$  plane of the 6 main groups identified in Fig. 10 as well as various individual, more isolated clusters. *Left:* Each ellipse shows the approximate locus of the 6 tentative main groups identified. *Right:* Location of independent clusters (with labels #1, #2, #3, #4, and #68). Each substructure is colour-coded as in Fig. 10, while the independent clusters are colour-coded arbitrarily. As discussed in Sect. 5.2, substructure B occupies the region dominated by Thamnos1+2, substructure C that of *Gaia*-Enceladus, D corresponds to Sequoia, and E to the Helmi streams. The orientation of substructure F is peculiar, and may indicate that its constituent clusters #65 and #66 should be treated separately.

gular momentum space in a similar manner as our clusters #60 and #61, are the result of a resonance in the orbits of some of the stars in the streams. This effect is thus a consequence of the Galactic potential. We preliminary conclude that analyses such as those presented for the Helmi streams here, using the internal properties of the clusters identified by our algorithm, can help us in fully assessing and characterizing the different building blocks present in the Galactic halo near the Sun.

## 5.2. Relationship to previously detected substructures

There have been several attempts to identify kinematic substructures in the Milky Way halo after the *Gaia* data releases. Here we focus on three studies that have selected or identified multiple kinematic substructures using the data from *Gaia* DR2 (Koppelman et al. 2019a; Naidu et al. 2020; Yuan et al. 2020b). Fig. 13 presents the comparisons in the  $L_z - E$  space. Although the three comparison studies define kinematic substructures using  $L_z$  and

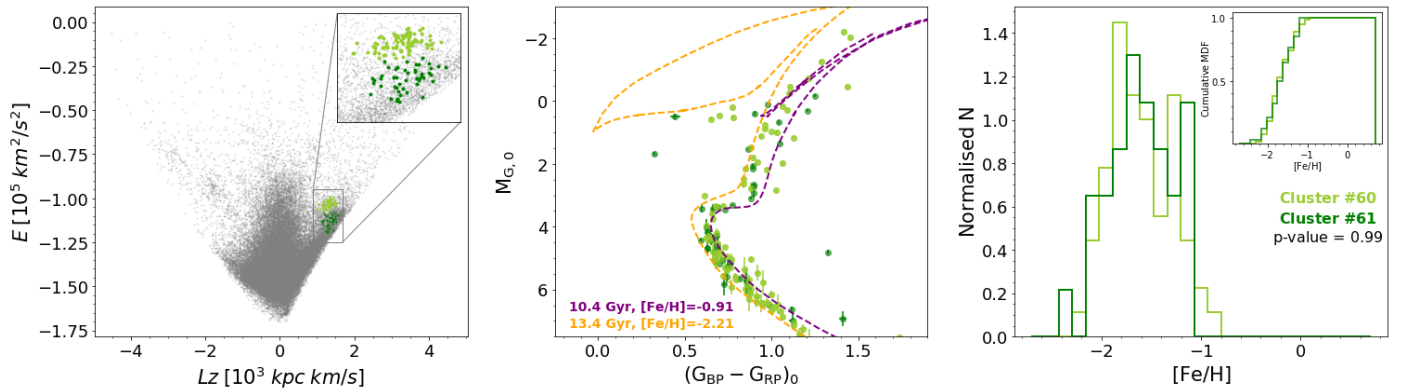


**Fig. 12.** Characterization of the Helmi streams as detected by the single linkage algorithm. *Left:* Distribution of the 51671 stars analysed in this work as well as clusters #60 and #61 (Helmi streams) in the  $E - L_z$  space. *Middle:* Colour-absolute Magnitude diagram for clusters #60 and #61. We overlay isochrones of a 10.4 Gyr ( $[\text{Fe}/\text{H}] = -0.91$ ) and a 13.4 Gyr ( $[\text{Fe}/\text{H}] = -2.21$ ) old populations from the updated BaSTI stellar evolution models (Hidalgo et al. 2018) in the *Gaia* EDR3 photometric system. *Right:* Metallicity distribution functions from LAMOST-LRS for clusters #60 and #61, where the cumulative distributions are shown in the inset.

$E$  and/or provide average  $L_z$  and  $E$  of the substructures, they adopted different Milky Way potentials (and slightly different position and velocity for the Sun). We therefore recompute  $L_z$  and  $E$  of the stars in the present study in the default Milky Way potential of the python package *gaia* (Price-Whelan 2017), which was used in Naidu et al. (2020), and in the Milky Way potential of McMillan (2016), which is used in the other two studies. Reassuringly, Fig. 13 shows that the clusters we identified remain tight even in these other Galactic potentials.

Based on the data from the H3 survey (Conroy et al. 2019), Naidu et al. (2020) investigated the properties of a number of substructures by defining selection boundaries simultaneously in dynamical and chemical spaces. Their sample consists of stars with heliocentric distance larger than 3 kpc, and therefore it is complementary to our study, which focuses on stars within 2.5 kpc from the Sun. Even though the spatial coverage is different, there is generally good agreement with our work; we find significant clusters with  $L_z$  and  $E$  close to the average properties of some structures from Naidu et al. (2020). However, we also find some differences for Aleph, Wukong, Thamnos, and Arjuna/Sequoia/I'toi.

In particular, we do not find significant clusters that would correspond to their Aleph and Wukong<sup>4</sup>. The absence of Aleph in our data is likely due to our  $|\mathbf{V} - \mathbf{V}_{\text{LSR}}| > 210 \text{ km/s}$  selection of halo stars, which would remove essentially all the stars on Aleph-like orbits. On the other hand, the reason for the absence of Wukong is less clear. Independently from Naidu et al. (2020), Yuan et al. (2020a) identified a stellar stream called LMS-1 from the analysis of K-giants from LAMOST DR6, which they associate with two globular clusters that Naidu et al. (2020) associate Wukong with. Since the findings by Yuan et al. (2020a) are based on stars with heliocentric distance of  $\sim 20 \text{ kpc}$  and since stars in Naidu et al. (2020) are also more distant than our sample, we may tentatively conclude that LMS-1/Wukong might be only prominent at larger distances than 2.5 kpc from the Sun (the distance limit of our sample). It therefore remains to be seen if the algorithm presented in this work confirms the existence of LMS-1/Wukong when it is applied to a sample with a larger volume coverage. We, however, note that clusters with  $2\sigma$  significance

do exist in the region of Wukong according to our single-linkage algorithm (see Figure 14).

We also find some differences when we compare the distribution of our significant clusters with Thamnos and Arjuna/Sequoia/I'toi as defined by Naidu et al. (2020). Our analysis has identified a group of clusters with retrograde motion and with low- $E$  that are clearly separated from *Gaia*-Enceladus, which would likely correspond to Thamnos according to the definition of Koppelman et al. (2019a), as discussed in the next paragraph. On the other hand, the average  $L_z$  and  $E$  of Thamnos by Naidu et al. (2020) are clearly different, occupying the region where we would probably associate clusters with *Gaia*-Enceladus as can be seen in the top panel of Fig. 13. In the region occupied by Arjuna/Sequoia/I'toi, which according to Naidu et al. (2020), contains three distinct structures with similar average kinematic properties but different characteristic metallicities, we also find significant clusters with a large retrograde motion and with large orbital energy. Two of our significant clusters (#62 and #63) that have similar  $L_z$  and  $E_n$  as Arjuna/Sequoia/I'toi, while another cluster (#64) clearly has different  $L_z$  and  $E_n$ , although also satisfies a more generous  $L_z - E_n$  selection criterion for retrograde structures by Naidu et al. (2020). We investigate the relationship between all these clusters in detail in Ruiz-Lara et al. (2022).

We now compare our clusters with the selections of *Gaia*-Enceladus, Sequoia, and Thamnos from Koppelman et al. (2019a). We find a number of significant clusters in the three regions identified by these authors to be associated with those objects. The analysis presented here (see bottom panel of Fig. 13) suggests that Sequoia might extend towards lower  $E$  and that the *Gaia*-Enceladus selection might also need to be shifted to lower  $E$ . It also suggests that Thamnos stars are more tightly clustered, although still in 2 significant clumps (see Ruiz-Lara et al. (2022)). In particular, the region originally occupied by the more retrograde Thamnos component (Thamnos 1 according to Koppelman et al. 2019a) appears fairly devoid of stars. This is partly due to the improvement in astrometry from *Gaia* DR2 to *Gaia* EDR3, especially the reduction in the zero-point offset from  $-0.054 \text{ mas}$  (Schönrich et al. 2019) to  $-0.017 \text{ mas}$  (Gaia Collaboration et al. 2021). Thamnos stars originally identified by Koppelman et al. (2019a) appeared to have lower  $L_z$  and higher  $E_n$  due to the underestimated parallaxes in DR2.

<sup>4</sup> Although several clusters (#12, #27, #39, #52, and #54) have some stars in the Wukong selection box, they are located at the edge of the box. We do not find any clusters that have similar values of  $L_z$  and  $E$  as the average values of Wukong stars from Naidu et al. (2020)



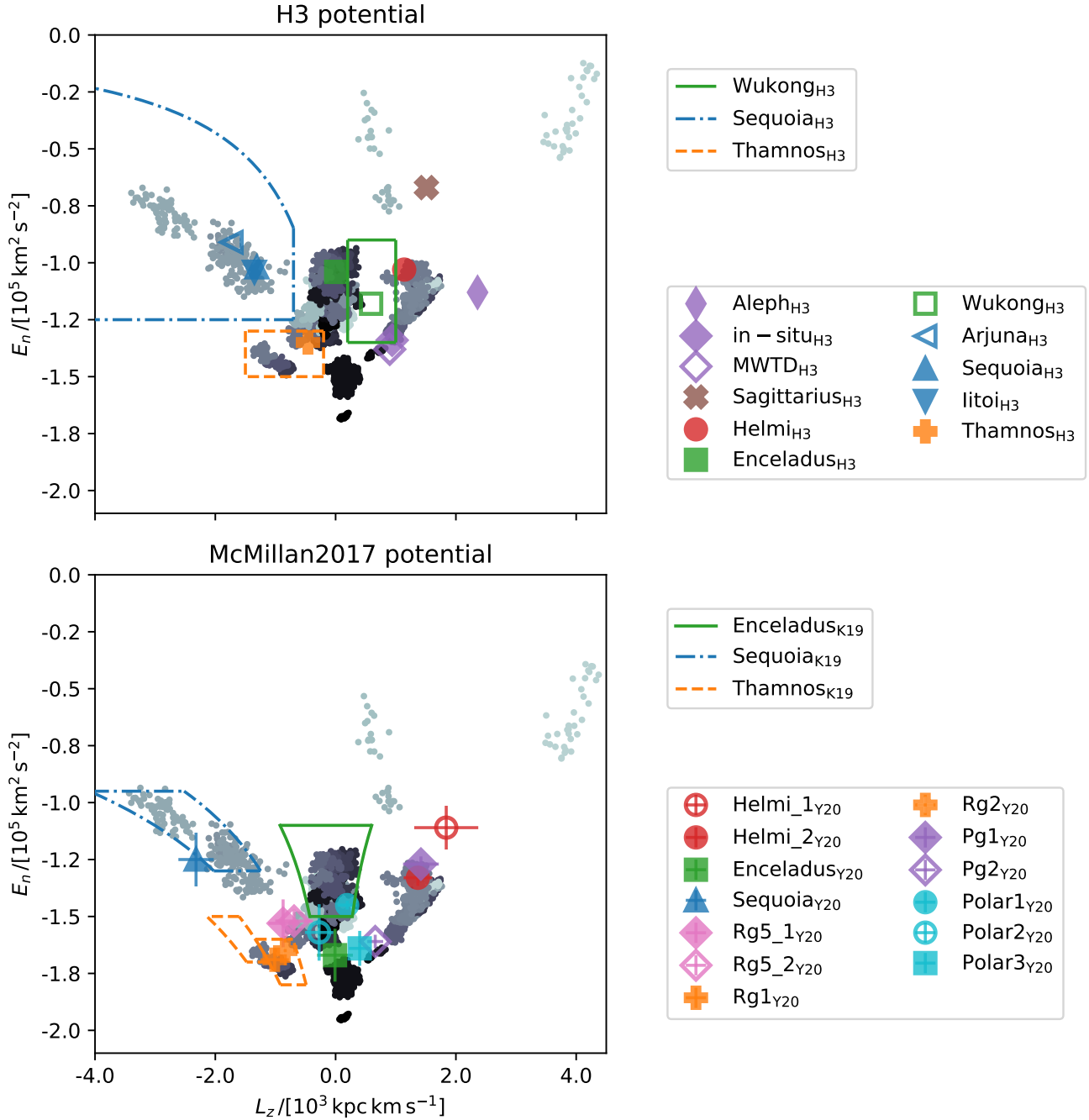


**Fig. 13.** Comparison of the clusters identified in the present work with those in the literature. The  $L_z$  and  $E$  of the stars in the clusters have been re-calculated for consistent comparisons (see text for details). While the upper panel provides a comparison with the results from the H3 survey (Naidu et al. 2020), the bottom panel presents comparisons with selection boundaries from Koppelman et al. (2019a) and the average kinematic properties of the substructures from Yuan et al. (2020a).

Yuan et al. (2020b) identified dynamically-tagged groups (DTGs) by applying a neural network-based algorithm, StarGO (Yuan et al. 2018), on a sample of very metal-poor stars ( $[\text{Fe}/\text{H}] < -2$ ) within 5 kpc from the Sun from LAMOST DR3 (Li et al. 2018). This implies that their results are more sensitive to the existence of kinematic substructures with low average metallicity. Here we compare our analysis with their DTGs that they associate with established structures (*Gaia*-Enceladus, the Helmi streams, *Gaia*-Enceladus, and Sequoia) and Rg5 from Myeong et al. (2018), and DTGs that they classified into sev-

eral groups depending on their kinematic properties (Rg1, Rg2, Pg1, Pg2, Polar1, Polar2, and Polar3)<sup>5</sup>. We find significant clusters that have nearly the same  $L_z$  and  $E$  as many of the groups these authors have identified. There are however, small offsets between the locations of our clusters and those of the other group they associated with the Helmi streams, their Sequoia, and *Gaia*-

<sup>5</sup> Yuan et al. (2020b) do not provide separate names for each component of retrograde/prograde/polar groups. We added a number so that we can distinguish them in Fig. 13 and compare them more straightforwardly to our own clusters.

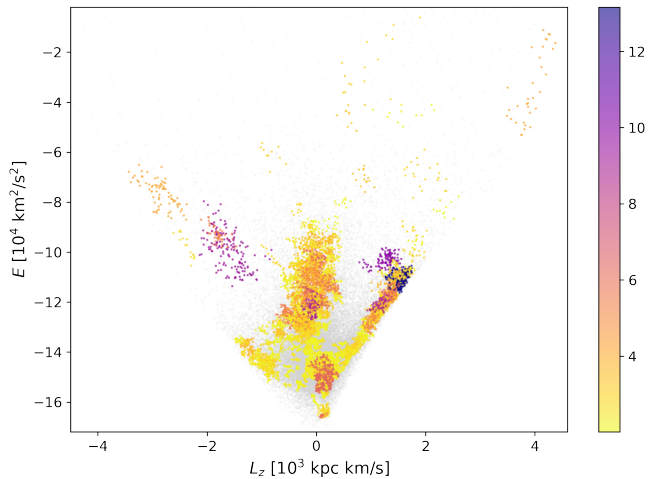


**Fig. 14.** Clusters identified by the single-linkage algorithm having at least  $2\sigma$  significance. They are colour coded according to their statistical significance. See for comparison Fig. 5.

Enceladus. These offsets might be due to the combined effects of differences in the sample, especially in metallicity and heliocentric distance, and in the method for cluster identification.

### 5.3. Structures with lower statistical significance

Fig. 14 displays clusters in the data set with a significance level of at least  $2\sigma$ . There are 362 clusters identified at this level, with 11150 (21.6 %) original members. There are in total 11311 stars (21.9 %) within a Mahalanobis distance of 2.13 to one of the  $2\sigma$  significance clusters.

A large number of the stars in the clusters with significance between 2 and  $3\sigma$  are located in the region between *Gaia*-Enceladus and the "hot" thick disk in  $E - L_z$  space. This densely populated region makes it harder to identify highly significant overdensities in comparison with our randomized data sets. Thus one may argue that the additional clusters of lower significance may be interesting in any case. A possible way to assess a more realistic level of acceptable statistical significance, could be to train the algorithm on simulations such that one can maximise the ratio of extracted signal to undesired false positives.

### 5.4. Summary

Our single linkage algorithm has identified 67 statistically significant clusters in Integrals of Motion space, many of which are rather compact in extent. The discussions of the previous sections suggest that they can be tentatively grouped into six main independent substructures, with some room for further splitting as well as merging (see Ruiz-Lara et al. (2022)).

It is worth noting that our algorithm tends to extract many local overdensities within what we would associate to a single accreted object on the basis of the discussions presented in Secs. 5.1 and 5.2. On the one hand, this could be due to the true morphology of the accreted object in Integrals of Motion space, which is expected to be split in substructures corresponding to individual streams crossing a local volume (see e.g. Gómez et al. 2010). On the other hand, it could be related to the difficulty in obtaining a high statistical significance for accreted objects with a large extent in Integrals of Motion space. For example, in the case of *Gaia*-Enceladus, one may argue that this is due to

the steep gradient in the density of stars in the Integrals of Motion space, particularly in energy. The single linkage algorithm generally links stars with higher binding energy *earlier* in the merging process because there are more such stars. From there it will form connected components that will grow towards lower binding energies. Thus the region occupied by *Gaia*-Enceladus is likely to be contaminated by high binding energy stars linked in such a way that the statistical significance of the less bound stars in what could be the *Gaia*-Enceladus region is never evaluated on its own.

A large number of clusters (although smaller than reported here) have also been found by Yuan et al. (2020b) using *Gaia* DR2 data. It is perhaps not so surprising that the improvement in the astrometry provided by *Gaia* EDR3 data has led to the discovery of even more substructures. Nonetheless, it is likely that we have not identified *all* the individual kinematic streams in our data set even after application of the HDBSCAN algorithm in velocity space on our single-linkage clusters. The velocity dispersions of the 232 (HDBSCAN) subgroups (see Fig. 8) are somewhat higher than expected for individual streams (Helmi & White 1999), although in part this could be due to orbital velocity gradients present because of the finite volume considered. Our ability to distinguish such moving groups is probably restricted by the number of stars (see Sec. 4.2). Furthermore, as discussed earlier, the region of low  $E$  and low  $L_z$ , given its high stellar density, is particularly hard to disentangle.

## 6. Conclusions

We have constructed a sample of halo stars within 2.5 kpc from the Sun using astrometry from *Gaia* EDR3, and radial velocities from *Gaia* DR2 supplemented with data from various ground-based spectroscopic surveys. Our goal has been to systematically identify substructures in Integrals of Motion space that could tentatively be associated with merger events. To this end we have applied the single linkage algorithm, which returns a set of connected components or potential clusters in the data set. We determined the statistical significance of each of these candidate clusters by comparing the observed density of the cluster with that of an artificially generated halo, obtained by scrambling the velocity components of our real halo set. As a statistical significance threshold we required that the density within an ellipsoidal contour covering 95% of the cluster distribution to be more than three standard deviations away from the mean expected density of the artificial data sets. Our final cluster labels were extracted by tracing all (possibly hierarchically overlapping) significant clusters in the merging tree and selecting the nodes where the statistical significance is maximized. In this way, we have identified 67 statistically significant clusters.

To obtain an indication of how likely it is for a star in our data set to belong to a cluster we have modelled each cluster as a Gaussian probability density. We then determined the Mahalanobis distance between any star and the cluster. As a guidance, a Mahalanobis distance of  $D_{\text{cut}} \sim 2.13$  roughly contains 80% of the stars in a cluster, and therefore this value can be used to identify "core members" which may be interesting for follow-up. We have found that  $\sim 13.8\%$  of the stars in our sample can be associated to a significant cluster according to this criterion.

Our findings are summarized in Table 1 and Table 2, which list respectively, the characteristics of the substructures and the stars dynamical properties together with their Mahalanobis distances. These tables are made available in electronic format upon publication, when we will also release the source codes on Github.

We also have identified subgroups in velocity space ( $v_R, v_\phi, v_z$ ) by applying the HDBSCAN algorithm separately on each statistically significant cluster. In this way, we extract 232 streams, some of which clearly correspond to subgroups resulting from a stream wrapping around its orbit being observed as it crosses a local volume.

Furthermore, we have also investigated the internal relationship between the clusters and how they map to previously established structures. We have tentatively been able to group the clusters into roughly 6 main independent structures leaving aside a number of independent clusters. Their characterisation and interrelation will be the focus of our paper II (Ruiz-Lara et al. 2022). In that work, we scrutinize their reality in detail, in terms of e.g. consistency in stellar populations, chemical abundances, and metallicity distributions. We may conclude that we have made significant steps towards a robust characterization of the substructure present in the halo near the Sun.

**Acknowledgements.** We use Python and the following libraries to implement our method in code: Vaex, for efficient handling of the data set and data exploration (Breddels & Veljanoski 2018). Scipy, for implementation of the single linkage algorithm and chi-square distribution (Virtanen et al. 2020). HDBSCAN for extracting substructure in velocity space (McInnes et al. 2017) and NumPy and Matplotlib for utility functions (Harris et al. 2020; Hunter 2007). We gratefully acknowledge financial support from a Spinoza prize from the Netherlands Organisation for Scientific Research (NWO) and HHK gratefully acknowledges financial support from the Martin A. and Helen Chooljian Membership at the Institute for Advanced Study. This work has made use of data from the European Space Agency (ESA) mission *Gaia* (<https://www.cosmos.esa.int/gaia>), processed by the *Gaia* Data Processing and Analysis Consortium (DPAC, <https://www.cosmos.esa.int/web/gaia/dpac/consortium>). Funding for the DPAC has been provided by national institutions, in particular the institutions participating in the *Gaia* Multilateral Agreement. This work also made use of the Third Data Release of the GALAH Survey (Buder et al. 2021). The GALAH Survey is based on data acquired through the Australian Astronomical Observatory. We acknowledge the traditional owners of the land on which the AAT stands, the Gamilaraay people, and pay our respects to elders past and present. This paper has made as well use of APOGEE DR16 data part of the SDSS IV scheme. Funding for the Sloan Digital Sky Survey IV has been provided by the Alfred P. Sloan Foundation, the U.S. Department of Energy Office of Science, and the Participating Institutions. We have made use of RAVE data for this work, see the RAVE web site at <https://www.rave-survey.org>. Guoshoujing Telescope (the Large Sky Area Multi-Object Fiber Spectroscopic Telescope LAMOST) is a National Major Scientific Project built by the Chinese Academy of Sciences. Funding for the project has been provided by the National Development and Reform Commission. LAMOST is operated and managed by the National Astronomical Observatories, Chinese Academy of Sciences.

## References

- Ahumada, R., Prieto, C. A., Almeida, A., et al. 2020, *ApJS*, 249, 3
- Belokurov, V., Erkal, D., Evans, N. W., Koposov, S. E., & Deason, A. J. 2018, *MNRAS*, 478, 611
- Belokurov, V., Sanders, J. L., Fattahi, A., et al. 2020, *MNRAS*, 494, 3880
- Belokurov, V., Zucker, D. B., Evans, N. W., et al. 2006, *ApJ*, 642, L137
- Bernard, E. J., Ferguson, A. M. N., Schlafly, E. F., et al. 2016, *MNRAS*, 463, 1759
- Binney, J. & McMillan, P. J. 2016, *MNRAS*, 456, 1982
- Borsato, N. W., Martell, S. L., & Simpson, J. D. 2020, *Monthly Notices of the Royal Astronomical Society*, 492, 1370
- Breddels, M. A. & Veljanoski, J. 2018, *Astronomy & Astrophysics*, 618, A13
- Buder, S., Sharma, S., Kos, J., et al. 2021, *MNRAS*[arXiv:2011.02505]
- Campello, R. J., Moulavi, D., & Sander, J. 2013, in *Pacific-Asia conference on knowledge discovery and data mining*, Springer, 160–172
- Conroy, C., Bonaca, A., Cargile, P., et al. 2019, *ApJ*, 883, 107
- Di Matteo, P., Haywood, M., Lehnert, M. D., et al. 2019, *A&A*, 632, A4
- Dodd, E., Helmi, A., & Koppelman, H. H. 2021, arXiv e-prints, arXiv:2105.09957
- Efstathiou, G., Frenk, C. S., White, S. D., & Davis, M. 1988, *Monthly Notices of the Royal Astronomical Society*, 235, 715
- Ester, M., Kriegel, H.-P., Sander, J., Xu, X., et al. 1996, in *Kdd*
- Everitt, B. S., Landau, S., Leese, M., & Stahl, D. 2011, *Cluster analysis 5th ed*
- Gaia Collaboration, Babusiaux, C., van Leeuwen, F., et al. 2018a, *A&A*, 616, A10
- Gaia Collaboration, Brown, A. G. A., Vallenari, A., et al. 2018b, *A&A*, 616, A1
- Gaia Collaboration, Brown, A. G. A., Vallenari, A., et al. 2021, *A&A*, 649, A1
- Gómez, F. A., Helmi, A., Brown, A. G., & Li, Y.-S. 2010, *Monthly Notices of the Royal Astronomical Society*, 408, 935
- Gómez, F. A., Helmi, A., Cooper, A. P., et al. 2013, *MNRAS*, 436, 3602
- Gower, J. C. & Ross, G. J. 1969, *Journal of the Royal Statistical Society: Series C (Applied Statistics)*, 18, 54
- Harris, C. R., Millman, K. J., van der Walt, S. J., et al. 2020, *Nature*, 585, 357
- Helmi, A. 2020, arXiv preprint arXiv:2002.04340
- Helmi, A., Babusiaux, C., Koppelman, H. H., et al. 2018, *Nature*, 563, 85
- Helmi, A. & de Zeeuw, T. P. 2000, *Monthly Notices of the Royal Astronomical Society*, 319, 657
- Helmi, A., Veljanoski, J., Breddels, M. A., Tian, H., & Sales, L. V. 2017, *Astronomy & Astrophysics*, 598, A58
- Helmi, A., White, S. D., De Zeeuw, P. T., & Zhao, H. 1999, *Nature*, 402, 53
- Helmi, A. & White, S. D. M. 1999, *MNRAS*, 307, 495
- Hidalgo, S. L., Pietrinferni, A., Cassisi, S., et al. 2018, *ApJ*, 856, 125
- Hunter, J. D. 2007, *Computing in science & engineering*, 9, 90
- Ivezić, Ž., Goldston, J., Finlator, K., et al. 2000, *AJ*, 120, 963
- Koppelman, H., Helmi, A., & Veljanoski, J. 2018, *The Astrophysical Journal Letters*, 860, L11
- Koppelman, H. H., Helmi, A., Massari, D., Price-Whelan, A. M., & Starkenburg, T. K. 2019a, *Astronomy & Astrophysics*, 631, L9
- Koppelman, H. H., Helmi, A., Massari, D., Roelenga, S., & Bastian, U. 2019b, *Astronomy & Astrophysics*, 625, A5
- Lallement, R., Capitanio, L., Ruiz-Dern, L., et al. 2018, *A&A*, 616, A132
- Lane, J. M. M., Bovy, J., & Mackereth, J. T. 2021, arXiv e-prints, arXiv:2106.09699
- Li, H., Tan, K., & Zhao, G. 2018, *ApJS*, 238, 16
- Liu, N., Fu, J.-N., Zong, W., et al. 2019, *Research in Astronomy and Astrophysics*, 19, 075
- Majewski, S. R., Skrutskie, M. F., Weinberg, M. D., & Ostheimer, J. C. 2003, *ApJ*, 599, 1082
- Massari, D., Koppelman, H. H., & Helmi, A. 2019, *A&A*, 630, L4
- Mateu, C., Read, J. I., & Kawata, D. 2018, *MNRAS*, 474, 4112
- McInnes, L., Healy, J., & Astels, S. 2017, *The Journal of Open Source Software*, 2
- McMillan, P. J. 2016, *Monthly Notices of the Royal Astronomical Society*, stw2759
- Myeong, G., Evans, N., Belokurov, V., Sanders, J., & Koposov, S. 2018, *Monthly Notices of the Royal Astronomical Society*, 478, 5449
- Myeong, G. C., Evans, N. W., Belokurov, V., Amorisco, N. C., & Koposov, S. E. 2018, *MNRAS*, 475, 1537
- Naidu, R. P., Conroy, C., Bonaca, A., et al. 2020, *The Astrophysical Journal*, 901, 48
- Ostdiek, B., Necib, L., Cohen, T., et al. 2020, *A&A*, 636, A75
- Price-Whelan, A. M. 2017, *The Journal of Open Source Software*, 2, 388
- Prusti, T., De Bruijne, J., Brown, A. G., et al. 2016, *Astronomy & Astrophysics*, 595, A1
- Rodriguez, M. Z., Comin, C. H., Casanova, D., et al. 2019, *PloS one*, 14, e0210236
- Ruiz-Lara, T., Matsuno, T., Lövdal, S. S., et al. 2022, arXiv e-prints, arXiv:2201.02405, Paper II
- Sanderson, R. E., Wetzel, A., Loebman, S., et al. 2020, *ApJS*, 246, 6
- Schönrich, R., Binney, J., & Dehnen, W. 2010, *Monthly Notices of the Royal Astronomical Society*, 403, 1829
- Schönrich, R., McMillan, P., & Eyer, L. 2019, *MNRAS*, 487, 3568
- Simpson, C. M., Gargiulo, I., Gómez, F. A., et al. 2019, *MNRAS*, 490, L32
- Springel, V., White, S. D., Jenkins, A., et al. 2005, *nature*, 435, 629
- Steinmetz, M., Guiglion, G., McMillan, P. J., et al. 2020a, *AJ*, 160, 83
- Steinmetz, M., Matijević, G., Enke, H., et al. 2020b, *AJ*, 160, 82
- Taylor, M. B. 2005, in *Astronomical Society of the Pacific Conference Series*, Vol. 347, *Astronomical Data Analysis Software and Systems XIV*, ed. P. Shopbell, M. Britton, & R. Ebert, 29
- Taylor, M. B. 2006, in *Astronomical Society of the Pacific Conference Series*, Vol. 351, *Astronomical Data Analysis Software and Systems XV*, ed. C. Gabriel, C. Arviset, D. Ponz, & S. Enrique, 666
- Vasiliev, E. 2019, *MNRAS*, 482, 1525
- Virtanen, P., Gommers, R., Oliphant, T. E., et al. 2020, *Nature Methods*, 17, 261
- Wang, J., Fu, J.-N., Zong, W., et al. 2020, *ApJS*, 251, 27
- Yanny, B., Newberg, H. J., Kent, S., et al. 2000, *ApJ*, 540, 825
- Yuan, Z., Chang, J., Banerjee, P., et al. 2018, *The Astrophysical Journal*, 863, 26
- Yuan, Z., Chang, J., Banerjee, P., et al. 2018, *ApJ*, 863, 26
- Yuan, Z., Chang, J., Beers, T. C., & Huang, Y. 2020a, *ApJ*, 898, L37
- Yuan, Z., Myeong, G. C., Beers, T. C., et al. 2020b, *ApJ*, 891, 39